Graphene on cubic and hexagonal SiC: A comparative theoretical study

O. Pankratov,* S. Hensel, P. Götzfried, and M. Bockstedte

Lehrstuhl für Theoretische Festkörperphysik, Universität Erlangen-Nürnberg, Staudtstrasse 7 B2, D-91058 Erlangen, Germany

(Received 28 June 2012; published 17 October 2012)

Epitaxial graphene grows on different SiC polytypes possessing distinct bulk band gaps. In this work we systematically investigate the influence of polytypes on the graphene electronic spectrum employing local-density approximation (LDA)/Heyd-Scuseria-Ernzerhof (HSE) *ab initio* calculations including different buffer layer–graphene layer stackings. We find a variation of the Dirac point position with respect to the valence-band edge as a function of the polytype hexagonality. HSE values are in good agreement with recent experimental results, while LDA corroborates the trends. Since the Dirac point, interface-related states, and the Fermi level follow similar polytype-induced shifts, the doping of the epilayer stays practically the same. For the AB stacked buffer and epilayer on a Si-terminated SiC substrate the graphene spectrum exhibits a polytype-dependent energy gap ϵ_g which ranges 25–40 meV for different polytypes. On the contrary, for the AA stacking the Dirac cone remains intact. We suggest a symmetry-based analytical model which explains the origin of the gap and its absence for the AA geometry and provides a direct connection between ϵ_g and the buffer-epilayer interaction potential.

DOI: 10.1103/PhysRevB.86.155432 PACS number(s): 73.22.Pr, 72.80.Vp, 73.20.−r

I. INTRODUCTION

SiC is a remarkable substrate which supports a self-organized epitaxial graphene growth.[1,2] At elevated temperature, mostly silicon atoms evaporate leading to a carbon enrichment of the surface. In the course of annealing, the excess carbon atoms form an epitaxial graphene layer. In the case of a Si-terminated SiC substrate, this layer rests on a carbon buffer layer.[3–6] The latter has a hexagonal structure similar to an ideal graphene sheet but distorted to match the underlying substrate. In spite of its graphene-like atomic geometry, the buffer layer does not possess the peculiar to graphene Dirac-Weyl cone-shaped bands at the corners of the Brillouin zone. In the buffer layer, the electron π states which are responsible for the Dirac-Weyl spectrum of an isolated graphene strongly interact with the substrate. This interaction erases the Dirac-Weyl features of the electron spectrum.[7–10] On the C-face of SiC no buffer layer has been clearly identified yet, although recently a buffer-like intermediate layer was reported.[11] Due to a much faster growth, one usually obtains here multilayered stacks of mutually rotated carbon layers.[2,12]

To date, most experimental studies of epitaxial graphene were performed on the hexagonal polytype 6H as well as 4H-SiC. Recently, the cubic polytype 3C-SiC has attracted increasing attention.[13–15] The latter is anticipated to be advantageous due to the better compatibility with the common cubic semiconductors, most importantly silicon. One expects that owing to a weak graphene-substrate coupling the influence of a particular polytype on graphene electronic structure is marginal. However, the band structures of the polytypes themselves differ substantially as reflected by a notable band gap variation from $\varepsilon_g^{2H} = 3.33$ eV to $\varepsilon_g^{3C} = 2.39$ eV.[16] This should lead to a different alignment of the Dirac-Weyl cone with the energy bands of a substrate. On the other hand, a similar surface geometric structure of the polytypes suggests a similar interface electronic structure and hence a similar Fermi-level pinning mechanism. The latter determines the epilayer doping.[1,2,8–10,17]

In this paper, we address the polytype influence on electronic properties of graphene epilayers such as the Dirac cone splitting and the Fermi-level pinning. We employ a simplified structural model of the SiC-graphene interface which is most suitable for a Si-terminated substrate where the existence of a well-defined buffer layer has been firmly established. For comparison, we consider in parallel the C-terminated case assuming a similar buffer layer structure.

Being in registry with a Si-terminated SiC surface the epitaxial graphene layer is subject to a spatial modulation such that the unit cell becomes 13×13 in terms of graphene translational period. This unit cell almost exactly coincides with the $(6\sqrt{3} \times 6\sqrt{3})R30$ surface cell,[3,4,18] a hallmark of reconstruction experienced by the carbon-rich Si-terminated SiC surface. This coincidence ensures the graphene-substrate commensuration. Alternatively, the commensuration condition can be satisfied via an approximate coincidence of the $\sqrt{13} \times \sqrt{13}$ graphene and the 5×5 SiC surface cells.[19] The 5×5 SiC reconstruction is, however, rarely observed[5,20,21] and, in practice, the $6\sqrt{3} \times 6\sqrt{3}$ structure dominates. Total-energy calculations[22] confirm that this structure is, indeed, the most stable amongst the possible low-stress interfaces. Unfortunately, the size of the $6\sqrt{3} \times 6\sqrt{3}$ cell is prohibitively large for *ab initio* band-structure calculations. A simpler, yet clearly idealized alternative to achieve commensuration is stretching the graphene layer by 8%, which makes it commensurate with the $(\sqrt{3} \times \sqrt{3})R30$ SiC surface cell. In spite of its simplicity, this model captures most essential features of the interface electron spectrum.[8–10] Due to the relatively small unit cell it is computationally tractable in contrast to the $6\sqrt{3} \times 6\sqrt{3}$ structure. This leads us to choose this model for the purpose of comparison of graphene electron spectrum on different SiC polytypes.

We report the results of the density functional theory calculations with local-density approximation (LDA) and Heyd-Scuseria-Ernzerhof (HSE06) functionals for a graphene epilayer on four SiC polytypes, for different surface terminations and different buffer-graphene stackings. In the most

interesting case of the AB stacking we find a Dirac cone splitting between 25 and 40 meV depending on the polytype. On the contrary, for AA stacking the Dirac cone remains intact. To understand these results we develop an analytical model based on symmetry arguments. We show that indeed, the energy gap occurs for the AB stacked epilayer, whereby the gap width ϵ_g is a measure of interaction of the graphene π states with the interface potential. The model also makes evident that for the AA stacking symmetry forbids the gap opening. These results are practically polytype independent, because, within the model, only the buffer and the underlying substrate atomic layer contribute to the interaction with graphene. The polytype is, however, essential for the alignment of the Dirac-Weyl bands with the SiC band structure. From the *ab initio* data we demonstrate a clear dependence of the Dirac point location within the SiC band gap on polytype hexagonality. Its value obtained for the HSE functional is in good agreement with recent experiments for 4H and 6H SiC,[23,24] while the LDA results corroborate the trends.

II. STRUCTURAL MODEL AND CALCULATIONAL METHOD

We consider one or two carbon monolayers (i.e., the buffer layer or the buffer layer plus graphene layer) on four SiC polytypes 2H, 4H, 6H, and 3C. The polytypes range from the purely hexagonal 2H to the purely cubic 3C structure. In the calculations, it is convenient to treat the 3C polytype on the same footing as the hexagonal polytypes using the associated "3H" unit cell. The matching of the $\sqrt{3} \times \sqrt{3}$ SiC surface unit cell with the 2×2 graphene cell is achieved by stretching the graphene layer.

Both graphene and SiC surfaces possess hexagonal reciprocal lattices and hexagonal Brillouin zones (BZs) [cf. Fig. 1(a)]. Within the $\sqrt{3} \times \sqrt{3}$ model, the graphene 1×1 BZ and the BZ of the $\sqrt{3} \times \sqrt{3}$ structure are rotated by 30° relative to the 1×1 SiC BZ. The correspondence of the high-symmetry points is shown in Fig. 1(b). In the 1×1 SiC lattice the conduction-band minimum (CBM) is situated in the M point for all considered polytypes except 2H, where it is in the K point. The valence-band maximum (VBM) is always in the Γ point.

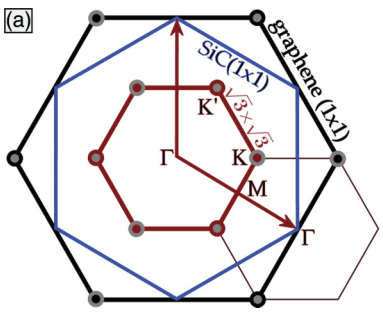

$SiC_{1\times1}$	↦	$SiC_{\sqrt{3}\times\sqrt{3}}$
K_{SiC}		Γ
M_{SiC}		M
$graphene_{1\times1}$	↦	$SiC_{\sqrt{3}\times\sqrt{3}}$
K_g		K
M_g		Γ

FIG. 1. (Color online) (a) The first Brillouin zones for 1×1 SiC (blue), 8% strained 1×1 graphene (black) and $\sqrt{3} \times \sqrt{3}$ SiC (red) structures. The correspondence of the high-symmetry points is shown in panel (b). The reciprocal-lattice vectors of the $\sqrt{3} \times \sqrt{3}$ SiC surface cell are shown in red.

TABLE I. Calculated (LDA, HSE) and experimental band gaps from Ref. 16 (E_g^{LDA}, E_g^{HSE}, and E_g^{exp}) of SiC polytypes (in eV).

	2H	4H	6H	3C
E_g^{LDA}	2.16	2.17	1.97	1.30
E_g^{HSE}	3.18	3.17	2.94	2.24
E_g^{exp}	3.33	3.27	3.02	2.39

We use a simulation supercell with either six (2H, 6H, 3C) or eight (4H) SiC bilayers. On top of the SiC slab one or two carbon layers are placed in either AB or AA stacking. To suppress the interaction of the periodic slab replicas we separate them by more than 10 Å. The dangling bonds on the bottom of the slab are saturated with hydrogen atoms.

We use the density functional program package VASP[25] with the local-density approximation (LDA).[26] The projected augmented wave potentials (PAWs)[27] describe the electron-ion interaction. Calculations were performed using Γ-centered **k**-grids which include the K point and plane-wave basis set with large energy cutoff (for details cf. Ref. 28). Prior to the electronic structure calculations the atomic geometry was optimized using the LDA functional until forces were smaller than 0.01 eV/Å.

The calculated structural parameters of the pH-SiC polytypes (a, c)[29] are in good agreement with theoretical[30] and experimental[16,31,32] data. Due to the well-known LDA overbinding, the lattice parameters are slightly smaller than experimental values but the ratios c/pa are consistent with experimental results. Similar agreement is obtained for the HSE06 functional.

In Table I the fundamental energy gaps of the SiC polytypes are listed. In comparison with experimental data[16] the calculated LDA gaps are underestimated by about 1.1 eV almost independent of the polytype, which is a well-known deficiency of the functional. The HSE06 functional, on the other hand, yields band gaps in fairly good agreement with the experiment. Such agreement is also obtained by more rigorous quasiparticle calculations.[33–37] Full-fledged quasiparticle (and even DFT-HSE06) calculations would be prohibitively expensive within the scope of the present work. Thus we confront a dilemma: on the one hand, we need to correctly pinpoint the Dirac spectrum relative to the substrate band structure which requires much more elaborate calculations than LDA. On the other hand, we aim at surveying a large variety of structures (different polytypes and graphene-buffer stackings) which is only possible if the computational effort stays at a manageable level. Our strategy for resolving the dilemma involves a combination of the LDA calculation with the hybrid functional HSE approach.[38,39] The latter is known to provide accurate single-particle energies at higher but still manageable computational cost. Following this strategy, we perform a limited set of the HSE calculations and use these data to benchmark the LDA bands. As expected, LDA spectra show the accurate band dispersion and the orderly trends along the polytype series. The position of the LDA gap edges are corrected by adjusting them to the HSE values in selected **k**-points using the vacuum potential as a common energy reference.

III. NUMERICAL RESULTS

In this section, we present *ab initio* results for graphene on Si- and C-terminated substrates of four SiC polytypes (3C, 6H, 4H, 2H). In particular, we address the Dirac cone position for two substrate terminations (Secs. III A and III B) and the Dirac cone splitting for different buffer-graphene stackings (Sec. III C).

A. Graphene epilayer on a Si-terminated substrate

In the $\sqrt{3} \times \sqrt{3}$ model,[8–10] the first carbon (buffer) layer binds covalently to the Si-terminated surface such that two of three surface Si-atoms are bonded to C-atoms leaving a single silicon dangling bond per surface unit cell. The shortest distance between buffer C-atoms and the surface Si-atoms varies between 1.97 Å (2H) and 1.99 Å (3C) which clearly speaks for a covalent bonding. As the carbon π electrons are involved in covalent bonding, it is not a surprise that the buffer layer does not possess Dirac-type bands at the Fermi level [cf. Figs. 2(a)–2(d)].

An important feature of the band structure in Fig. 2 is the half-filled flat interface band which pins the Fermi level. The pinning persists when the second carbon layer (i.e., epitaxial graphene) is placed on top of the buffer. Now, the Dirac cone emerges in the SiC band gap. It is clearly seen that graphene is n-doped [cf. Figs. 2(e)–2(h)]. Note that these properties are found with the LDA as well as with the HSE06 functionals. The discussion focuses first on the DFT-LDA band structures with its high **k**-point density along the path. Subsequently, we turn to the HSE06 bands as given at the special **k**-points Γ, M, and K. The band alignment between LDA and the HSE06 in Fig. 2 was accomplished by using the vacuum potential as the common energy reference.

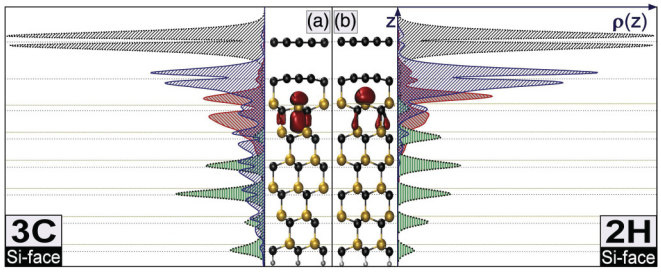

FIG. 3. (Color online) The (x,y)-averaged electron density along the slab z-axis for AB stacked graphene-buffer on Si-terminated 3C and 2H substrates. The charge density $\rho(z) = \int |\Psi|^2 dxdy$ is shown for the Dirac states in the K point (black), for the "lower cone" states in the K point (blue; these states merge with the valence band in the 3C case) and for the interface band at E_F (red) [cf. Figs. 2(e) and 2(h)]. In green, the bulk Γ state at the VBM is shown. Middle panels show the 3C (a) and 2H (b) slab geometries and charge contours of the interface states in the K point. Horizontal dashed lines indicate the average atomic positions within each layer.

To reveal the origin of the band structure in Fig. 2 we inspect the electron density distributions along the z-direction normal to the slab surface for different states. The in-plane averaged densities $\rho(z) = \int |\Psi(x,y,z)|^2 \, dxdy$ for electron states in the K point are depicted in Fig. 3. It is clearly seen that, indeed, the states at the apex of the Dirac cone are formed by the π orbitals of epitaxial graphene layer. Interestingly, a

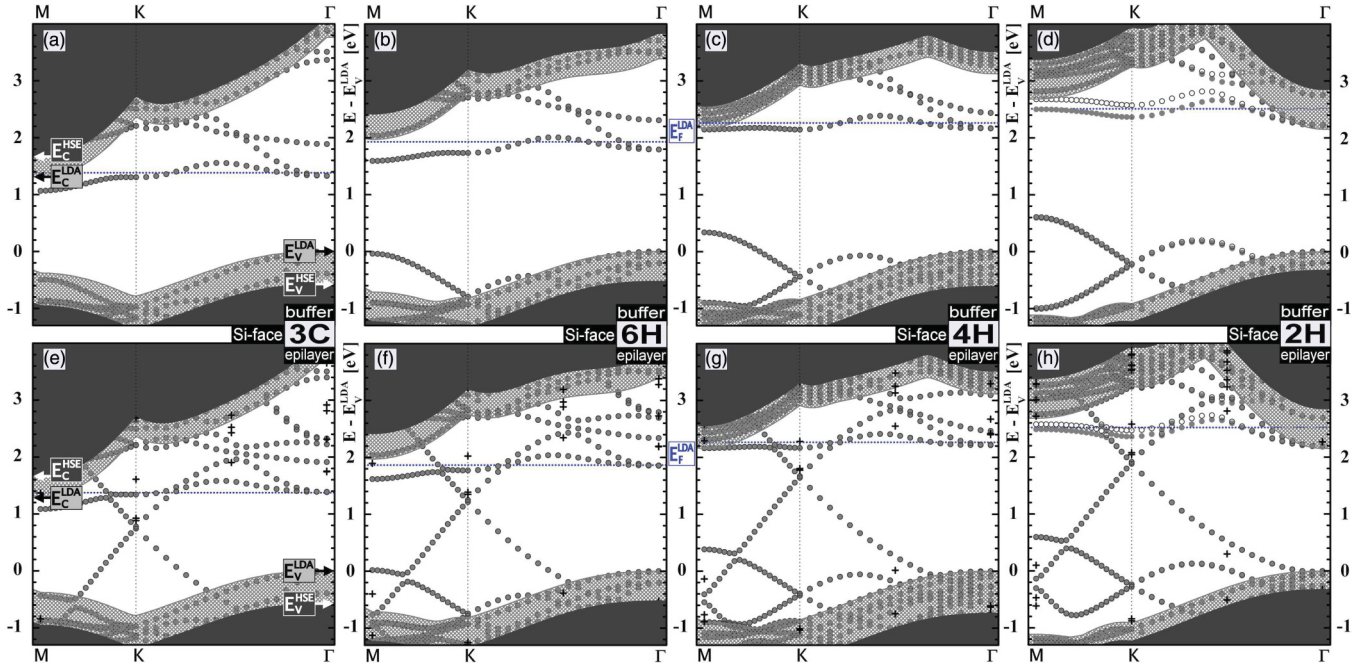

FIG. 2. (Color online) Calculated band structures for the buffer layer (top panel) and the graphene-buffer stack (bottom panel) on SiC substrates. All substrates are Si-terminated and the epilayer-buffer stacking is of AB type. The DFT-LDA projected bulk bands are indicated by gray shaded regions. The black shaded regions show the projected HSE band structure obtained by LDA data adjustment to the HSE band edges. The LSDA graphene cone and the interface states are shown by open and filled circles representing the opposite spin states. A slight spin splitting occurs only in the 2H case [panels (d) and (h)]. The HSE data points are shown as black crosses. The Fermi level E_F is indicated by the dotted blue line.

similar density distribution (shown in blue) which is located immediately below the graphene layer belongs to a "buried cone" overlapping with the valence band [cf. Figs. 2(e)–2(h)]. It essentially derives from the residual π orbitals of the buffer layer which do not participate in covalent bonding. Next follow the interface states (shown in red) which are responsible for the Fermi-level pinning. Finally, the bulk state propagating through the whole slab is shown in green, which is identified with the VBM state at the Γ point.

The Dirac cone featured in the lower panel of Fig. 2 is almost the same as in a free standing graphene, which signifies that the states at the cone apex practically do not interact with the substrate except for a small splitting of the cone (see below). Close to the Fermi energy, however, the Dirac states show a weak interaction with interface states. This interaction causes an avoided crossing of the bands. Yet this effect is suppressed due to a spatial separation of the Dirac states and the interface states (cf. Fig. 3). A similar weak hybridization was found in a 5×5 supercell calculation for epitaxial graphene on 2H-SiC.[19] Figures 2(e)–2(h) make evident a systematic shift of the Dirac point (the cone apex) along the considered polytype sequence. We address this trend in more detail in Sec. III C.

The analysis of the HSE06 bands and their charge density obtained at the high-symmetry points Γ, M, and K reveals the same assignment to interface, buffer, and graphene states as for the LDA states within its band gap. In particular we find that the HSE and LDA Dirac point fall almost on top of each other after electrostatic potential alignment in the vacuum region. Also the Fermi-level pinning by the interface states is preserved, although the interface band position is shifted to slightly higher energies ($\lesssim$0.3 eV). Due to the pinning by the interface state, the Fermi level (not shown in Fig. 2) is located at a slightly higher energy than the LDA. Compared to the LDA band structure, the largest effect of the HSE is the opening of the band gap, which affects both the valence and conduction bands, in agreement with earlier quasiparticle calculations.[35] This asymmetric opening largely corrects the position of the interface state and of the Dirac point with respect to the valence-band edge. For the polytypes 4H and 6H experiments measured the position of the Dirac point relative to the valence-band maximum of 2.91 ± 0.1 eV (Ref. 23) and 2.25 eV (Ref. 24) in good agreement with the HSE values of 2.53 and 1.9 eV (cf. Table II). This agreement underlines the relevance of our simplified $\sqrt{3} \times \sqrt{3}$ interface model for polytype-related trends. The theoretical values are somewhat smaller due to the model-dependent strain effect or the HSE error.

B. Graphene epilayer on the C-terminated substrate

In contrast to the Si-terminated surface, the graphene formation on the C-terminated SiC does not happen via the carbon-rich $6\sqrt{3} \times 6\sqrt{3}$ surface reconstruction. Due to a much faster growth, it is very difficult (albeit possible)[40,41] to obtain a monolayer graphene. Usually, one deals with stacks of tens to hundreds of mutually rotated graphene layers.[12,42] The different growth mode on the C-face reflects a different bonding situation. No well-defined buffer layer was found so far, with an exception of a recent communication[11] where an interlayer similar to that on a Si-terminated surface was observed. Still, the well-documented decoupling of a graphene epilayer from the substrate, which is on the C-face even more pronounced than on the Si-face, requires some sort of a buffer-type interface ingredient preventing the direct covalent bonding between the epilayer and the surface. Silicon adatoms were considered as alternatives for the carbon buffer layer in theoretical studies.[43]

In this paper, we adopt for the C-face an interface model with the same carbon buffer layer as on the Si-face. On one hand, it is instructive to compare similar interface configurations for both substrate terminations. On the other hand, the buffer interface model for the C-termination bears, quiet remarkably, universal features which are characteristic to the real graphene epilayer on the C-face of SiC. Most importantly, it describes a much weaker graphene-substrate interaction than on the Si-face, which is reflected by an extremely small splitting of the Dirac cone (cf. Sec. III C). Other features such as the large spin splitting of the interface state and the graphene charge neutrality are clearly model dependent.

Figure 4 shows the energy bands for the AB buffer-graphene stack on C-terminated substrates. In contrast to the Si-terminated case, the interface state is shifted towards the VBM and exhibits a large spin splitting of about 1 eV. The Dirac energy E_D falls in the spin-split gap and hence no charge transfer between the substrate and the epilayer occurs. This situation persists for all considered SiC polytypes.

TABLE II. Calculated values of the Dirac cone splitting ϵ_g (in meV), the position of the Dirac point with respect to the valence-band edge $E_D - E_V$ (in eV), and the Dirac point position relative to the Fermi energy $E_F - E_D$ (in eV) for two exchange-correlation functionals. Experimental values for $E_D - E_V$ are given where available. All data refer to Bernal (AB) graphene-buffer stacking. Note an extremely small cone splitting on the C-face.

	Si-face			Si-face			C-face	
SiC	ϵ_g^{LDA}	$E_D^{LDA} - E_V^{LDA}$	$E_F^{LDA} - E_D^{LDA}$	ϵ_g^{HSE}	$E_D^{HSE} - E_V^{HSE}$	$E_D^{Exp} - E_V^{Exp}$	ϵ_g^{LDA}	$E_D^{LDA} - E_V^{LDA}$
3C	36.7	0.76	0.62	41.4	1.48		1.7	0.66
6H	35.4	1.23	0.64	39.9	1.90	2.25[a]	1.4	0.62
4H	26.3	1.66	0.61	28.0	2.53	2.91 ± 0.1[b]	1.4	0.42
2H	32.9	1.90	0.62	33.9	2.39		1.7	0.24

[a]Reference 24.

[b]Obtained from $E_C - E_D = 0.36 \pm 0.1$ eV given in Ref. 23.

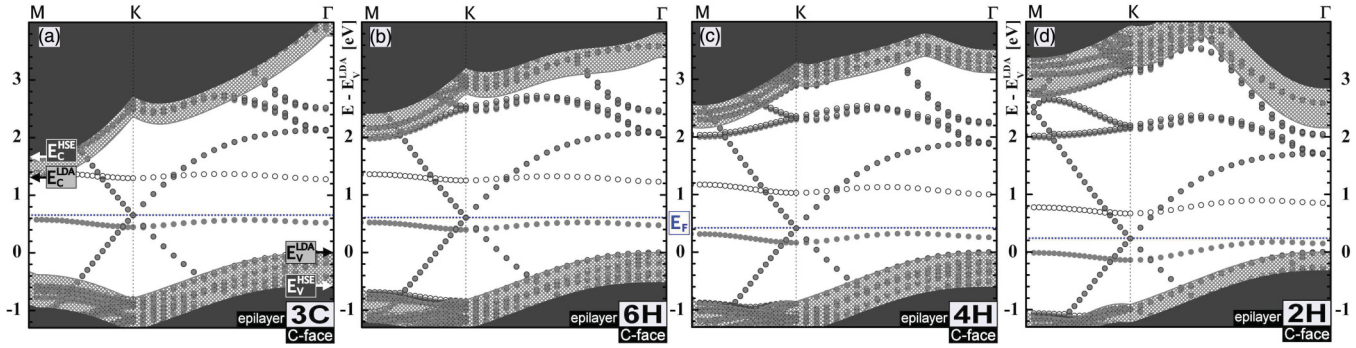

FIG. 4. (Color online) Calculated band structure of AB buffer-graphene stack on the C-terminated substrates of four SiC polytypes. Only LSDA data points are shown. The energy zero is taken at the LSDA bulk VBM (E_V) in Γ. The black shaded region shows the projected HSE band structure obtained by adjustment of the LDA data to the HSE band edges. The Fermi level E_F is indicated by the dotted blue line and the different spin states are shown by closed and open circles.

C. Dirac spectrum

Figures 2 and 4 corroborate the most important property of the buffer-graphene stacks on SiC—the maintenance of the Dirac spectrum similar to that of a free standing graphene. In this section, we focus on a small energy window around the Dirac point E_D to reveal (i) the Dirac state dispersion close to E_D and (ii) the evolution of the Dirac point position along the polytype series.

Let us address the E_D position first. Figure 5 shows E_D and the Fermi level E_F as functions of polytype hexagonality. In the pH-polytype there are two hexagonal bilayers and $(p-2)$ cubically stacked bilayers. The ratio $2/p$ is introduced as the hexagonality, which vanishes in the 3C case by definition. In other words, the parameter of hexagonality reflects the density of wurzite-type bilayer stackings in the material. It varies between 0 for the cubic 3C-SiC and 1 for the "most hexagonal" 2H-SiC.

As evident from Fig. 5(a), the separation between the Dirac point and the valence-band maximum systematically *increases* when going to polytypes with larger hexagonality for graphene on Si-terminated substrates. On the contrary, it *decreases* for a C-termination. The latter circumstance, although derived for an idealized interface model, signifies that the upwards trend

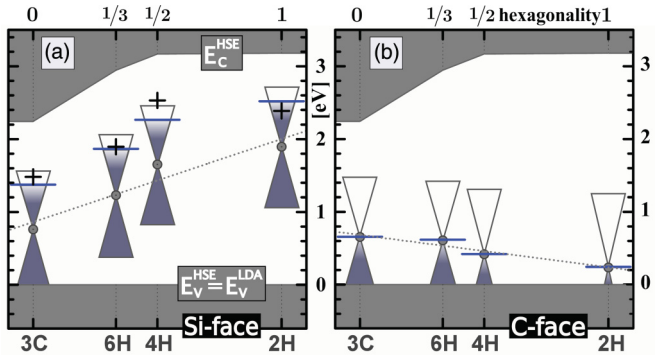

FIG. 5. (Color online) The Dirac point position (circles) and the Fermi level (blue) relative to the VBM (E_V) along a sequence of polytypes for (a) Si- and (b) C-terminated substrates. The HSE data for the Dirac point position [panel (a)] is shown as black crosses. The polytype hexagonality is plotted on the horizontal axis.

for the Si-terminated substrates is most probably unrelated to the systematic increase of the SiC band gap.

The calculated shift of E_D (cf. Table II) compares well with experimental data available for 4H and 6H polytypes $(E_D - E_V)^{4H} \simeq 2.91 \pm 0.1$ eV[23] and $(E_D - E_V)^{6H} \simeq 2.25$ eV.[24] A comparison with Figs. 2 and 4 favors the suggestion that E_D is linked to the interface state rather than to the bulk gap edges. Since E_F is pinned by the same interface state [as seen already for the buffer layer system in Figs. 2(a)–2(d)], the Fermi-level position relative to E_D and consequently the epilayer doping remain unchanged through the polytype series (cf. Fig. 5). We find the Dirac point 0.62 eV below the Fermi level for the $\sqrt{3} \times \sqrt{3}$ interface model (cf. Table II) compared to 0.41 eV for the 5×5 (Ref. 19) and 0.32 eV for the $6\sqrt{3} \times 6\sqrt{3}$ (Ref. 18) structures and 0.45 eV in experiments.[24,44] Respectively, for the electron density we have $n \simeq 5.6 \times 10^{13}\,\mathrm{cm}^{-2}$ for the $\sqrt{3} \times \sqrt{3}$ and $n \simeq 2.8 \times 10^{13}\,\mathrm{cm}^{-2}$ for the 5×5 models.[19] For the $6\sqrt{3} \times 6\sqrt{3}$ structure Kim *et al.*[18] reported $8.7 \times 10^{12}\mathrm{cm}^{-2}$ (obtained with a Mullikan analysis). The experimental value is $10^{13}\,\mathrm{cm}^{-2}$.[1,44] It is instructive to calculate the spatially resolved electron populations within the SiC-buffer-graphene system to visualize the charge transfer responsible for the doping. With the Bader population analysis[45,46] we obtain for the electron density in graphene $3.2 \times 10^{13}\,\mathrm{cm}^{-2}$. The small difference with the number resulting from the Fermi-level position should be attributed to the overlap between the buffer- and graphene-related states which influences the charge separation in the Bader analysis. The difference of the Bader populations of the buffer layer with and without on-top graphene yields $\Delta n \simeq 2.5 \times 10^{13}\,\mathrm{cm}^{-2}$ which is reasonably close to the doping value obtained for the graphene epilayer. This analysis confirms that the n-type doping of the graphene epilayer stems from the Fermi-level pinning by the interface states essentially located in the buffer layer. This mechanism holds for *all* polytypes and *all* interface models for the Si-face.

In this context it is interesting to compare the work functions of the free standing graphene layers (strained and unstrained) and for the buffer-SiC surface. We find that the 8% strain increases the graphene work function from 4.5 to 5.1 eV (and alters the Fermi velocity, see below). For the $\sqrt{3} \times \sqrt{3}$ buffer-SiC surface we obtain 4.0 eV and hence the work function difference amounts to 1.1 eV if the strained graphene value

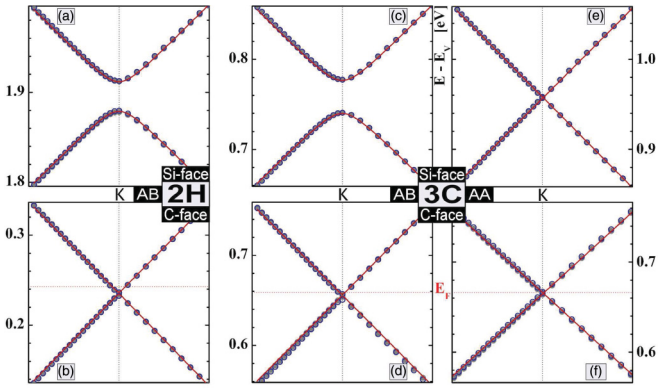

FIG. 6. (Color online) High-resolution spectra of a graphene epilayer in the range of $[\frac{1}{20}\overline{MK}, \frac{1}{20}\overline{K\Gamma}]$. Shown are the DFT-LSDA results obtained on the Si- and C-face (top and bottom panels) and 2H and 3C polytypes for different stackings [AB type (a)–(d) and AA type (e) and (f)]. Solid red lines are the fitting curves according to Eq. (1) with $v_F = 0.84 v_F^0$ (see text).

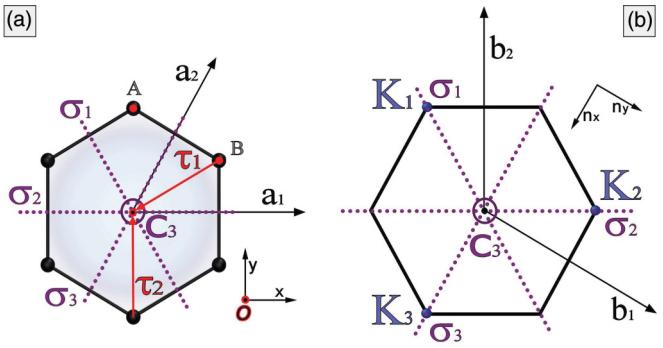

FIG. 7. (Color online) Hexagonal unit cell of a graphene lattice (a) with translation vectors $\mathbf{a}_{1,2}$ and symmetry planes σ. (b) The Brillouin zone with reciprocal-lattice translations $\mathbf{b}_{1,2}$ and the equivalent points K_μ.

is used. Curiously, this number is in good agreement with experiment.[23] It is also close to the work function difference of ∼1 eV used in Ref. 47 to reproduce the graphene n-doping with a simple electrostatic model. This indicates that the error due to simplification of the interface structure is partly compensated by the error due to the artificial graphene stretching.

Figure 6 shows a close-up of the Dirac bands. The high-resolution spectra are obtained in the interval $[\frac{1}{20}\overline{MK}, \frac{1}{20}\overline{K\Gamma}]$ around the K point. The AB stacked graphene-buffer structure on the Si-face clearly possesses a band gap $\epsilon_g^{\mathrm{LDA}}$ which ranges between 26.3 meV (4H) and 36.7 meV (3C) depending on the polytype (cf. Table II). A similar splitting of the Dirac bands was calculated within the strain-free 5×5 interface model.[19] On the contrary, the Dirac bands in graphene on the C-face exhibit a vanishing gap for all polytypes, which is within the computational error margins. This reflects an extreme weakness of the graphene-substrate interaction in this case. Quite remarkably, no Dirac cone splitting occurs for the AA graphene-buffer stacking *regardless* of the substrate termination and the polytype [shown for 3C-SiC in Figs. 6(e) and 6(f)]. As shown in the next section, it is a straightforward consequence of a specific symmetry of the AA interface structure.

To extract the Fermi velocity v_F we fit the bands in Fig. 6 as

$$E(k;\epsilon_g, v_F) = \pm\sqrt{\left(\frac{\epsilon_g}{2}\right)^2 + (v_F \hbar k)^2}. \qquad (1)$$

The fitting curves shown in red all yield $v_F = 0.84\, v_F^0$ independently of the polytype and the surface termination, where $v_F^0 = 8.33 \times 10^5$ m/s is the calculated Fermi velocity of a free standing (unstrained) graphene layer. Note that v_F^0 is slightly lower than the experimental value of about 10^6 m/s which, however, is irrelevant for the notable suppression of v_F that we observe in our case. This suppression has its origin in the artificial 8% strain applied to the graphene layer within the $\sqrt{3} \times \sqrt{3}$ interface model. To verify this, we calculate v_F^s for an 8% strained free standing graphene sheet and, indeed, find $v_F^s = 0.87\, v_F^0$. This indicates that the interaction with the underlying buffer-SiC substrate has practically no influence on the Fermi velocity.

IV. SYMMETRY ANALYSIS

To understand the origin of the band gap in epitaxial graphene we perform a symmetry analysis of the energy spectrum. For our purposes, the explicit evaluation of the Hamiltonian is most convenient in a free electron basis. Here the basis functions at a K point are the symmetrized linear combinations of the plane waves $|\boldsymbol{K}_\mu\rangle$ of the three equivalent K points [cf. Fig. 7(b)] with wave vectors $\boldsymbol{k}_\mu$ ($\mu = 1,2,3$).

We will see that for a $\sqrt{3} \times \sqrt{3}$ interface the combination of both the buffer and the substrate potential is needed to lift the degeneracy at the K point. We find that the graphene-buffer stacking is important. Namely, it has to be AB type (Bernal) to induce a gap, whereas for AA stacking the degeneracy persists.

We start with the perfect isolated graphene sheet. Here the K point small group C_{3v} $\{E, 2C_3, 3\sigma\}$ contains, apart from the unit element E, two rotations around a trigonal axis at the origin O and three mirror planes $\sigma_{1,2,3}$ (cf. Fig. 7). The latter swap the neighboring lattice sites A and B [cf. Fig. 7(a)]. In contrast, rotations by the angle $\frac{\pm 2\pi}{3}$ around the trigonal axis express the equivalence of the A and B sites separately.

Due to the trigonal symmetry, the Hamiltonian matrix in the K point has the following form:

$$\widehat{H}_K = \begin{pmatrix} 0 & V & V^* \\ V^* & 0 & V \\ V & V^* & 0 \end{pmatrix} \qquad (2)$$

with

$$V = \langle \boldsymbol{K}_1 | V(\boldsymbol{r}) | \boldsymbol{K}_2 \rangle := |V| e^{i\varphi}, \qquad (3)$$

where V defines the matrix element of a crystalline potential. The matrix of Eq. (2) is brought to diagonal form by the unitary transformation

$$\widehat{S} = \frac{1}{\sqrt{3}} \begin{pmatrix} 1 & 1 & 1 \\ s & s^* & 1 \\ s^* & s & 1 \end{pmatrix} \text{ with } \quad s := e^{i(2\pi/3)} \qquad (4)$$

resulting in

$$\widehat{S}\,\widehat{H}_K\,\widehat{S}^\dagger = 2|V| \begin{pmatrix} \cos\varphi & 0 & 0 \\ 0 & \cos\left(\frac{2\pi}{3}-\varphi\right) & 0 \\ 0 & 0 & \cos\left(\frac{2\pi}{3}+\varphi\right) \end{pmatrix} =: \operatorname{diag}[\epsilon_1,\epsilon_2,\epsilon_3]. \tag{5}$$

The eigenfunctions $\Psi_{\mathbf{k}_\mu}$ belonging to eigenvalues ϵ_μ are

$$\begin{aligned} \Psi_{\boldsymbol{k}_1} &= \frac{1}{\sqrt{3}}\left(\Phi_{\boldsymbol{k}_1}+\Phi_{\boldsymbol{k}_2}+\Phi_{\boldsymbol{k}_3}\right), \\ \Psi_{\boldsymbol{k}_2} &= \frac{1}{\sqrt{3}}\left(s^*\,\Phi_{\boldsymbol{k}_1}+s\,\Phi_{\boldsymbol{k}_2}+\Phi_{\boldsymbol{k}_3}\right), \\ \Psi_{\boldsymbol{k}_3} &= \frac{1}{\sqrt{3}}\left(s\,\Phi_{\boldsymbol{k}_1}+s^*\,\Phi_{\boldsymbol{k}_2}+\Phi_{\boldsymbol{k}_3}\right), \end{aligned} \tag{6}$$

where

$$\Phi_{\boldsymbol{k}_\mu} := \exp\left(i\,\boldsymbol{k}_\mu \boldsymbol{r}\right) \quad (\mu = 1,2,3) \tag{7}$$

is the μth plane-wave basis state $|\boldsymbol{K}_\mu\rangle$ in $\boldsymbol{r}$-representation. If the plane waves are defined relative to the coordinate origin O in a hexagon center [cf. Fig. 7(a)], the eigenfunction $\Psi_{\boldsymbol{k}_1}$ has nodes on all lattice sites, whereas $\Psi_{\boldsymbol{k}_2}$ and $\Psi_{\boldsymbol{k}_3}$ have nodes on sites A or B, respectively.

The trigonal symmetry does not guarantee the degeneracy of two of three eigenvalues ϵ_μ in Eq. (5), for the phase $\varphi \in (-\pi,\pi)$ is arbitrary. In other words, if we had a trigonal axis only, the point group of a K point would be $C_3\,\{E,2C_3\}$ which possesses only one-dimensional irreducible representations. Adding the mirror planes (cf. Fig. 7) raises the symmetry to C_{3v}. This point group has two one-dimensional A_1, A_2 and one two-dimensional E representations. In fact, the mirror symmetry restricts the phase φ to values $\varphi \in \{0, \frac{\pm 2\pi}{3}\}$. The particular value of φ depends, however, on the coordinate origin O. With our choice in the hexagon center [cf. Fig. 7(a)] we have $\hat{\sigma}_3 \Phi_{\boldsymbol{k}_2} = \Phi_{\boldsymbol{k}_3}$ and $\langle\Phi_{\boldsymbol{k}_2}|\,V\,|\Phi_{\boldsymbol{k}_3}\rangle = \langle\Phi_{\boldsymbol{k}_3}|\,V\,|\Phi_{\boldsymbol{k}_2}\rangle$ and hence $\varphi \equiv 0$. Alternatively, the origin shift by $\boldsymbol{\tau}_2 = (0,d)$ to atom A, where d is the nearest-neighbor distance, generates the phase shifts of the basis functions via

$$\boldsymbol{k}_1\boldsymbol{\tau}_2 = \frac{2\pi}{3}, \quad \boldsymbol{k}_2\boldsymbol{\tau}_2 = 0, \quad \boldsymbol{k}_3\boldsymbol{\tau}_2 = -\frac{2\pi}{3}, \tag{8}$$

which yields $\varphi = \frac{-2\pi}{3}$. The shift by $\boldsymbol{\tau}_1$ of the origin to atom B makes $\varphi = \frac{+2\pi}{3}$. It is apparent from Eq. (5) that taking the different phase choices $\varphi = \{0 \to \frac{2\pi}{3} \to \frac{-2\pi}{3}\}$ corresponds to a cyclic permutation of the eigenvalues in Eq. (5) with the two lowest ones being degenerate. For $\varphi = 0$ these are $\epsilon_{2,3}$ and we have

$$\epsilon_1 = 2|V| \quad \text{and} \quad \epsilon_{2,3} = 2|V|\cos\left(\frac{2\pi}{3}\right) = -|V|. \tag{9}$$

Obtaining the spectrum in a close vicinity of a K point is straightforward. Introducing a small shift $\boldsymbol{k}$ from the K point we get, in addition to Eq. (2), the matrix

$$\widehat{H}_{\boldsymbol{k}} = \begin{pmatrix} \xi_1 & 0 & 0 \\ 0 & \xi_2 & 0 \\ 0 & 0 & \xi_3 \end{pmatrix}, \tag{10}$$

where $\xi_\mu = 3v_F\,\boldsymbol{k}\cdot\boldsymbol{n}_\mu$ $(\mu = 1,2,3)$ are energy shifts of the basis states. The unit vectors $\boldsymbol{n}_\mu = \frac{\boldsymbol{k}_\mu}{|\boldsymbol{k}_\mu|}$ point from the Brillouin-zone center to K_μ and v_{F} appears as the Fermi velocity in the Dirac-Weyl Hamiltonian (see below). The latter is obtained transforming Eq. (10) to the eigenstate basis of Eqs. (6),

$$\widehat{S}\,\widehat{H}_{\boldsymbol{k}}\,\widehat{S}^\dagger = \begin{pmatrix} 0 & p & p^* \\ p^* & 0 & p \\ p & p^* & 0 \end{pmatrix}. \tag{11}$$

Here we introduce the notation

$$p = s^*\,\xi_1 + s\,\xi_2 + \xi_3 = v_{\mathrm{F}}\,\boldsymbol{k}(\boldsymbol{n}_x + i\,\boldsymbol{n}_y) \tag{12}$$

with orthogonal vectors

$$\boldsymbol{n}_x = \boldsymbol{n}_3 - \frac{1}{2}(\boldsymbol{n}_1+\boldsymbol{n}_2) \quad \text{and} \quad \boldsymbol{n}_y = \frac{\sqrt{3}}{2}(\boldsymbol{n}_2-\boldsymbol{n}_1). \tag{13}$$

Now, considering the full Hamiltonian $\widehat{H}_K + \widehat{H}_{\boldsymbol{k}}$ in the eigenstate basis of $\widehat{H}_K$ [cf. Eqs. (6)] we obtain

$$\widehat{S}\,(\widehat{H}_K + \widehat{H}_{\boldsymbol{k}})\,\widehat{S}^\dagger = \begin{pmatrix} \epsilon_1 & p & p^* \\ p^* & \epsilon_2 & p \\ p & p^* & \epsilon_3 \end{pmatrix}. \tag{14}$$

The Dirac-Weyl Hamiltonian ($\widehat{H}_{\mathrm{DW}}$) arises when two of the three eigenvalues are degenerate. For example, in the case $\varphi = 0$ it is the lower right 2×2 block in the matrix (14),

$$\widehat{H}_{\mathrm{DW}} = \begin{pmatrix} -|V| & p \\ p^* & -|V| \end{pmatrix}. \tag{15}$$

The outlined view at the origin O of a graphene spectrum allows us to easily include the effect of a substrate. Since this effect is small, we describe the interaction with the substrate via a perturbation potential $v(\boldsymbol{r})$ which accounts only for the buffer and the last atomic layer of a substrate [cf. Fig. 8(a)]. This makes, together with the epitaxial graphene layer, a three layer system which altogether possesses a trigonal symmetry axis. In the case of the AB graphene-buffer stacking, there are no mirror planes. Hence the small group of K becomes C_3 and the degenerate level at the apex of the Dirac cone must split giving rise to the band gap. On the contrary, for AA stacking the C_{3v} symmetry is preserved and no gap is expected.

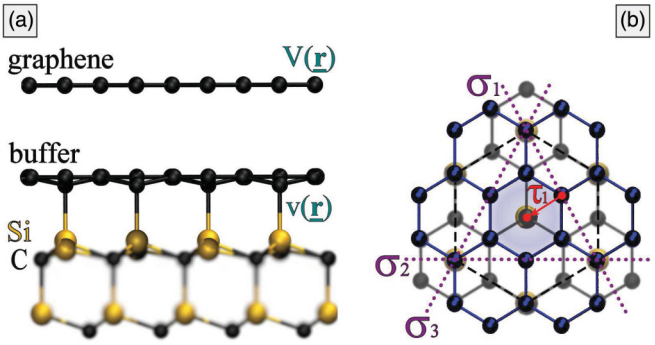

FIG. 8. (Color online) (a) Side and (b) top views of a Si-terminated substrate with two carbon layers (AB stacking). The top view (b) shows, along with graphene epilayer (blue circles), the underlying buffer (grey circles) and last Si-layer (yellow circles) of the substrate.

To evaluate the splitting of the Dirac cone we need a perturbation matrix $\hat{v}$. Due to the trigonal symmetry it reads similar to Eq. (2),

$$\hat{v} = \begin{pmatrix} 0 & v & v^* \\ v^* & 0 & v \\ v & v^* & 0 \end{pmatrix} \tag{16}$$

with

$$v = \langle \boldsymbol{K}_\mu | \, v(\boldsymbol{r}) \, | \boldsymbol{K}_\nu \rangle := |v| \, e^{i\chi}, \tag{17}$$

where the phase χ of the matrix element is important, since it determines the cone splitting. This phase can be revealed in a following way. Although the whole three-layer structure does not have mirror symmetries, the potential $v(\boldsymbol{r})$ is symmetric with respect to reflections in planes $\sigma_{1,2,3}$ [cf. Fig. 8(b)]. These planes, however, do not intersect in a single point and do not run through the coordinate origin O in the hexagon center with respect to which the basis functions (7) are defined. Hence these reflection operations involve translations by vectors $2\boldsymbol{\tau}_\mu$ [cf. Fig. 8(b)]. For example,

$$\begin{aligned} \widehat{\sigma}_1 \Phi_{\boldsymbol{k}_1} &= e^{-2i\,\boldsymbol{k}_1\boldsymbol{\tau}_1} \, \Phi_{\boldsymbol{k}_1}, \\ \widehat{\sigma}_1 \Phi_{\boldsymbol{k}_2} &= e^{-2i\,\boldsymbol{k}_2\boldsymbol{\tau}_1} \, \Phi_{\boldsymbol{k}_3}, \\ \widehat{\sigma}_1 \Phi_{\boldsymbol{k}_3} &= e^{-2i\,\boldsymbol{k}_3\boldsymbol{\tau}_1} \, \Phi_{\boldsymbol{k}_2}, \end{aligned} \tag{18}$$

with $\boldsymbol{\tau}_1 = -\frac{a}{2}(\sqrt{3},1)$. For matrix elements (17) we find

$$v = \left\langle \Phi_{\boldsymbol{k}_2} \right| v(\boldsymbol{r}) \left| \Phi_{\boldsymbol{k}_3} \right\rangle = \left\langle \Phi_{\boldsymbol{k}_3} \right| v(\boldsymbol{r}) \left| \Phi_{\boldsymbol{k}_2} \right\rangle e^{2i(\boldsymbol{k}_2 - \boldsymbol{k}_3)\boldsymbol{\tau}_1} \tag{19}$$

and hence the phase $\chi = (\boldsymbol{k}_2 - \boldsymbol{k}_3)\boldsymbol{\tau}_1 = \frac{2\pi}{3}$. The matrix $\widehat{H}_K + \hat{v}$ which determines the energy levels in the K point has the same structure as Eqs. (2) and (16) but with the composite matrix elements

$$w = |V| + |v| \, e^{i(2\pi/3)} \simeq |V| + i\frac{\sqrt{3}}{2}|v| \simeq |V| \, e^{i\gamma} \tag{20}$$

with

$$\gamma \simeq \frac{\sqrt{3}}{2}\frac{|v|}{|V|} \ll 1. \tag{21}$$

Using Eq. (5) we find the band gap

$$\begin{aligned} \epsilon_g = \epsilon_2 - \epsilon_3 &= 2|V| \left[\cos\left(\frac{2\pi}{3} - \gamma\right) - \cos\left(\frac{2\pi}{3} + \gamma\right) \right] \\ &\simeq 2\sqrt{3}\,|V|\,\gamma = 3|v|. \end{aligned} \tag{22}$$

Apart from the cone splitting, the potential $v(\boldsymbol{r})$ causes a slight shift of the midgap energy

$$\frac{1}{2}(\epsilon_2 + \epsilon_3) = -|V|\left(1 - \frac{\gamma^2}{2}\right) = -|V| + \frac{3}{8}\frac{|v|^2}{|V|}. \tag{23}$$

The interface geometry depicted in Fig. 8 corresponds to the AB graphene-buffer stacking, which is observed on a Si-terminated SiC substrate. We see that in this case the Dirac cone is split, whereby the energy gap $\epsilon_g = 3|v| \approx 30$ meV gives an estimate for a graphene-substrate interaction strength $|v| \approx 10$ meV. If the stacking were of AA type, the three-layer structure would possess the full point symmetry of an ideal graphene sheet. In this case no phase shift in the matrix elements of Eqs. (17), (19), and (20) is generated and the degeneracy at the apex of the Dirac cone is preserved. The numerical calculations [cf. Figs. 6(e) and 6(f)] confirm this conclusion.

The symmetry analysis establishes a connection between the *ab initio* band-structure data and the model Hamiltonian close to the Dirac point. For the $\sqrt{3} \times \sqrt{3}$ model and for the strain-free 5×5 structure[19] it reveals a similar weak interaction of the Dirac electrons with the substrate resulting in a similar small Dirac cone splitting. Formally, the symmetry analysis cannot be directly transferred to the $6\sqrt{3} \times 6\sqrt{3}$ case because of a more complex geometry and the lower symmetry. Yet, the pronounced similarity of $\sqrt{3} \times \sqrt{3}$ and 5×5 cases let us conjecture that the similar small Dirac cone splitting occurs also for the $6\sqrt{3} \times 6\sqrt{3}$ interface. The extensive experimental data[1,44,48,49] strongly indicate that this splitting must be small, giving an upper limit of 40–50 meV. This estimate allows the splitting values that we find in our calculations. It definitely rules out a much larger value of 200 meV reported in a $6\sqrt{3} \times 6\sqrt{3}$ calculation by Kim *et al.*[18]

V. SUMMARY

In summary, we compared the band structures of graphene epilayers on different SiC polytypes with different surface terminations and buffer-graphene stackings. Combination of LDA- and HSE-based DFT calculations allowed us to obtain an alignment of the Dirac and projected-band spectra in agreement with available experimental data for the 4H and 6H polytypes. We find a systematic shift of the Dirac point and of the pinned Fermi level with the substrate hexagonality. Both increase relative to the valence-band maximum for graphene on the Si-terminated surface and decrease for the C-termination. The epilayer doping practically remains constant as the Fermi level relative to the Dirac point and the Fermi velocity are polytype independent. A small energy gap ϵ_g in the range between 25 and 40 meV is present in the Dirac spectrum of AB-stacked graphene-buffer structures on Si-terminated substrates. There is no gap for the AA stacking as well as for graphene layers on the C-face. The origin of the Dirac cone splitting ϵ_g as well as its absence for the AA stacking case can be understood within the analytical symmetry-based model. The model provides a direct connection between ϵ_g and the graphene-substrate coupling strength, which is rather weak (10 meV) and practically polytype independent.

ACKNOWLEDGMENTS

This work was supported by ESF under the program EuroGRAPHENE CRP GRAPHIC-RF (DFG Grant No. PA 516/8-1), the DFG special priority program "Graphene" (DFG Grant No. PA 516/9-1), and by the Collaborative Research Center SFB 953.

*oleg.pankratov@physik.uni-erlangen.de

[1] T. Seyller, A. Bostwick, K. V. Emtsev, K. Horn, L. Ley, J. L. McChesney, T. Ohta, J. D. Riley, E. Rotenberg, and F. Speck, Phys. Status Solidi B **245**, 1436 (2008).

[2] J. Hass, W. A. de Heer, and E. H. Conrad, J. Phys.: Condens. Matter **20**, 27 (2008).

[3] T. Seyller, K. Emtsev, K. Gao, F. Speck, L. Ley, A. Tadich, L. Broekman, J. Riley, R. Leckey, O. Rader, A. Varykhalov, and A. Shikin, Surf. Sci. **600**, 3906 (2006).

[4] G. M. Rutter, N. P. Guisinger, J. N. Crain, E. A. A. Jarvis, M. D. Stiles, T. Li, P. N. First, and J. A. Stroscio, Phys. Rev. B **76**, 235416 (2007).

[5] S. Nie and R. M. Feenstra, J. Vac. Sci. Technol. **27**, 1052 (2009).

[6] Y. Qi, S. H. Rhim, G. F. Sun, M. Weinert, and L. Li, Phys. Rev. Lett. **105**, 085502 (2010).

[7] C. Riedl, C. Coletti, T. Iwasaki, A. A. Zakharov, and U. Starke, Phys. Rev. Lett. **103**, 246804 (2009).

[8] A. Mattausch and O. Pankratov, Phys. Rev. Lett. **99**, 076802 (2007).

[9] A. Mattausch and O. Pankratov, Phys. Status Solidi B **245**, 1425 (2008).

[10] F. Varchon, R. Feng, J. Hass, X. Li, B. N. Nguyen, C. Naud, P. Mallet, J.-Y. Veuillen, C. Berger, E. H. Conrad, and L. Magaud, Phys. Rev. Lett. **99**, 126805 (2007).

[11] N. Srivastava, G. He, Luxmi, and R. M. Feenstra, Phys. Rev. B **85**, 041404 (2012).

[12] J. Borysiuk, J. Sołtys, R. Bożek, J. Piechota, S. Krukowski, W. Strupiński, J. M. Baranowski, and R. Stepniewski, Phys. Rev. B **85**, 045426 (2012).

[13] A. Ouerghi, M. Portail, A. Kahouli, L. Travers, T. Chassagne, and M. Zielinski, Mater. Sci. Forum **645–648**, 585 (2010).

[14] A. Ouerghi, R. Belkhou, M. Marangolo, M. Silly, S. Moussaoui, M. Eddrief, L. Largeau, M. Portail, and F. Sirotti, Appl. Phys. Lett. **97**, 161905 (2010).

[15] A. Ouerghi, M. Ridene, A. Balan, R. Belkhou, A. Barbier, N. Gogneau, M. Portail, A. Michon, S. Latil, P. Jegou, and A. Shukla, Phys. Rev. B **83**, 205429 (2011).

[16] K. H. Hellwege, O. Madelung, M. Schulz, H. Weiss, W. von Münch Landolt-Börnstein, New Series, vol. III/17a, Physics of group IV elements and III-V compounds (Springer-Verlag, Berlin, Heidelberg, New York, 1982).

[17] D. L. Miller, K. D. Kubista, G. M. Rutter, M. Ruan, W. A. de Heer, P. N. First, and J. A. Stroscio, Science **324**, 924 (2009).

[18] S. Kim, J. Ihm, H. J. Choi, and Y.-W. Son, Phys. Rev. Lett. **100**, 176802 (2008).

[19] O. Pankratov, S. Hensel, and M. Bockstedte, Phys. Rev. B **82**, 121416 (2010).

[20] P. Martensson, F. Owman, and L. Johansson, Phys. Status Solidi B **202**, 501 (1997).

[21] C. Riedl, U. Starke, J. Bernhardt, M. Franke, and K. Heinz, Phys. Rev. B **76**, 245406 (2007).

[22] G. Sclauzero and A. Pasquarello, Phys. Rev. B **85**, 161405 (2012).

[23] S. Sonde, F. Giannazzo, V. Raineri, R. Yakimova, J.-R. Huntzinger, A. Tiberj, and J. Camassel, Phys. Rev. B **80**, 241406 (2009).

[24] J. Ristein, S. Mammadov, and T. Seyller, Phys. Rev. Lett. **108**, 246104 (2012).

[25] G. Kresse and J. Furthmüller, Phys. Rev. B **54**, 11169 (1996).

[26] D. M. Ceperley and B. J. Alder, Phys. Rev. Lett. **45**, 566 (1980).

[27] P. E. Blöchl, Phys. Rev. B **50**, 17953 (1994).

[28] The extensive high-quality LDA band-structure calculations employed a $9 \times 9 \times 1$ **k**-grid and a plane-wave cutoff of 520 eV. For HSE calculations a $6 \times 6 \times 1$ **k**-grid and a lower cutoff energy 420 eV, which proved sufficient for that purpose.

[29] Calculated (and experimental from Refs. 16,31, and 32) structural parameters $(a, \frac{c}{pa})$ of the considered pH-SiC polytypes. Here 3C is represented in the hexagonal cell (3H), a is the lattice constant, and c is the lattice parameter perpendicular to the xy-plane of the slab surface. The LDA results are

$$\begin{aligned}
&3\mathrm{H}: a = 3.072\,(3.083)\,\text{Å}, \quad \frac{c}{pa} = 0.816\,(0.817),\\
&6\mathrm{H}: a = 3.062\,(3.073)\,\text{Å}, \quad \frac{c}{pa} = 0.817\,(0.818),\\
&4\mathrm{H}: a = 3.060\,(3.073)\,\text{Å}, \quad \frac{c}{pa} = 0.818\,(0.818),\\
&2\mathrm{H}: a = 3.058\,(3.076)\,\text{Å}, \quad \frac{c}{pa} = 0.820\,(0.821)
\end{aligned}$$

For the HSE06 functional we obtain, e.g., $a_{3\mathrm{H}} = 3.101$ Å and $a_{4\mathrm{H}} = 3.073$ Å. In view of the minor spread of the lattice constants we employ a common in-plane lattice constant $a_{3\mathrm{H}} = 3.072$ Å for all polytypes. The $\frac{c}{a}$ ratios were chosen identical to experimental values.

[30] M. C. Righi, C. A. Pignedoli, G. Borghi, R. Di Felice, C. M. Bertoni, and A. Catellani, Phys. Rev. B **66**, 045320 (2002).

[31] A. Bauer, J. Kräußlich, L. Dressler, P. Kuschnerus, J. Wolf, K. Goetz, P. Käckell, J. Furthmüller, and F. Bechstedt, Phys. Rev. B **57**, 2647 (1998).

[32] A. G. Zabrodskii, *New Semiconductor Materials. Characteristics and Properties*, Tech. Rep. (Ioffe Institute, 1998-2001) 26 Polytekhnicheskaya, St. Petersburg 194021, Rus. Fed., http://www.ioffe.rssi.ru/SVA/NSM/Semicond/SiC/basic.html.

[33] M. Rohlfing, P. Krüger, and J. Pollmann, Phys. Rev. B **48**, 17791 (1993).

[34] F. Bechstedt and P. Käckell, Phys. Rev. Lett. **75**, 2180 (1995).

[35] B. Wenzien, P. Käckell, F. Bechstedt, and G. Cappellini, Phys. Rev. B **52**, 10897 (1995).

[36] M. Shishkin and G. Kresse, Phys. Rev. B **75**, 235102 (2007).

[37] M. Shishkin, M. Marsman, and G. Kresse, Phys. Rev. Lett. **99**, 246403 (2007).

[38] A. V. Krukau, O. A. Vydrov, A. F. Izmaylov, and G. E. Scuseria, J. Chem. Phys. **125**, 224106 (2006).

[39] J. Paier, M. Marsman, K. Hummer, G. Kresse, I. C. Gerber, and J. G. Ángyán, J. Chem. Phys. **124**, 154709 (2006).

[40] W. A. de Heer, C. Berger, M. Ruan, M. Sprinkle, X. Li, Y. Hu, B. Zhang, J. Hankinson, and E. Conrad, PNAS **108**, 16900 (2011).

[41] X. Wu, Y. Hu, M. Ruan, N. K. Madiomanana, J. Hankinson, M. Sprinkle, C. Berger, and W. A. de Heer, Appl. Phys. Lett. **95**, 223108 (2009).

[42] J. Hass, F. Varchon, J. E. Millán-Otoya, M. Sprinkle, N. Sharma, W. A. de Heer, C. Berger, P. N. First, L. Magaud, and E. H. Conrad, Phys. Rev. Lett. **100**, 125504 (2008).

[43] L. Magaud, F. Hiebel, F. Varchon, P. Mallet, and J.-Y. Veuillen, Phys. Rev. B **79**, 161405 (2009).

[44] J. Jobst, D. Waldmann, F. Speck, R. Hirner, D. K. Maude, T. Seyller, and H. B. Weber, Phys. Rev. B **81**, 195434 (2010).

[45] R. Bader, *Atoms in Molecules: A Quantum Theory* (Oxford University Press, New York, 1990).

[46]G. Henkelman, A. Arnaldsson, and H. Jónsson, Comput. Mater. Sci. **36**, 354 (2006).
[47]S. Kopylov, A. Tzalenchuk, S. Kubatkin, and V. I. Fal'ko, Appl. Phys. Lett. **97**, 112109 (2010).
[48]T. Ohta, A. Bostwick, J. L. McChesney, T. Seyller, K. Horn, and E. Rotenberg, Phys. Rev. Lett. **98**, 206802 (2007).
[49]A. Bostwick, T. Ohta, T. Seyller, K. Horn, and E. Rotenberg, Nat. Phys. **3**, 36 (2007).